Draft version April 30, 2022
Typeset using LaTeX/show your work! twocolumn style in AASTeX631

Applying the metallicity-dependent binary fraction to double white dwarf formation: Implications for LISA

Sarah Thiele ,[1,2] Katelyn Breivik ,[3,2] and Robyn E. Sanderson [4,3]

[1]Department of Physics and Astronomy, University of British Columbia, 6224 Agricultural Road, Vancouver, BC, V6T 1Z1, Canada
[2]Canadian Institute for Theoretical Astrophysics, University of Toronto, 60 St. George Street, Toronto, Ontario, M5S 1A7, Canada
[3]Center for Computational Astrophysics, Flatiron Institute, 162 Fifth Ave, New York, NY, 10010, USA
[4]Department of Physics and Astronomy, University of Pennsylvania, 209 South 33rd Street, Philadelphia, PA 19104, USA

ABSTRACT

Short-period double white dwarf (DWD) binaries will be the most prolific source of gravitational waves (GWs) for the Laser Interferometer Space Antenna (LISA). DWDs with GW frequencies below ~ 1 mHz will be the dominant contributor to a stochastic foreground caused by overlapping GW signals, limiting the detectability of individual sources of all kinds. Population modeling of Galactic DWDs typically assumes a binary fraction of 50%. However, recent observations have shown that the binary fraction of close, solar-type stars exhibits a strong anti-correlation with metallicity. In this study we perform the first simulation of the Galactic DWD population observable by LISA which incorporates an empirically-derived metallicity-dependent binary fraction. We simulate DWDs using the binary population synthesis suite `COSMIC` and incorporate a metallicity-dependent star formation history to create a Galactic population of short-period DWDs. We compare two models: one which assumes a metallicity-dependent binary fraction, and one with a binary fraction of 50%. We find that while metallicity impacts the evolution and intrinsic properties of our simulated DWD progenitor binaries, the LISA-resolvable populations of the two models remain roughly indistinguishable. However, the size of the total Galactic DWD population orbiting in the LISA frequency band is reduced by more than half when accounting for a metallicity-dependent binary fraction. This effect lowers the confusion foreground, effectively increasing the sensitivity for detecting all types of low-frequency LISA sources. We repeat our analysis for three different assumptions for Roche-lobe overflow interactions and find the population reduction to be robust when a metallicity-dependent binary fraction is assumed.

Keywords: Binary stars — Stellar evolution — GW astronomy

1. INTRODUCTION

Most stars in the Galaxy will end their lives as white dwarfs. Of the stars which are born with a binary companion, many will undergo interactions which bring the two stars closer together, eventually forming a close double white dwarf (DWD). Close DWDs, with orbital periods shorter than ~ 2.75 hr are the largest source by number of mHz gravitational waves (GWs) in the Galaxy (e.g., Amaro-Seoane et al. 2017). The Laser Interferometer Space Antenna (LISA) is expected to resolve at least 10^4 individual DWD binaries in the Milky Way and will also observe GW emission from the entire Galactic DWD population through the unresolved foreground created by overlapping signals at sub-mHz frequencies (e.g., Nelemans et al. 2001; Ruiter et al. 2010; Nissanke et al. 2012; Yu & Jeffery 2013; Korol et al. 2017; Lamberts et al. 2019; Breivik et al. 2020b). The resolved population will enable the study of several important aspects of binary evolution like the strength of tides (Valsecchi et al. 2012) and the stability of mass transfer in DWD systems (e.g., Marsh et al. 2004; Shen 2015; Gokhale et al. 2007; Sepinsky & Kalogera 2014; Kremer et al. 2015) as well as provide a probe of Galactic structure (Korol et al. 2019) and the Local Group (Korol et al. 2018). The shape and strength of the Galactic DWD foreground can also be used as a tool to study the structure of the Milky Way (Benacquista &

Corresponding author: Sarah Thiele
sarahgthiele@gmail.com

Holley-Bockelmann 2006; Breivik et al. 2020a) as well as the separation distribution of close DWDs (Korol et al. 2021).

The transition between individually resolved DWDs and the confusion limited, or unresolved, DWD foreground is expected to occur near $\sim$ 1 mHz frequencies (e.g. Ruiter et al. 2010). In the confusion limited regime, more than one binary radiates GWs in each LISA frequency bin, thus creating a superposition of signals which are unable to be disentangled. There are multiple parameters which shape the Galactic DWD foreground. Assuming the evolution of each DWD system is driven solely by GW emission, the frequency derivative scales proportionally to $f_{\rm GW}^{11/3}$, causing a pileup of DWDs at lower frequencies (Breivik et al. 2019). The spatial density of DWDs in the Galaxy which defines the distance to each binary also impacts the foreground amplitude, since strain scales inversely with distance. Star formation history assumptions combine these two effects by assigning ages and positions to each DWD in the population which determine the present day orbital (and thus GW) frequencies as well as distances to each source.

When viewed strictly as a source of noise, the unresolved Galactic DWD foreground is the dominant noise source for LISA in the sub-mHz part of LISA's frequency range. This extra noise above the detector noise floor affects the detection of all other LISA sources including extreme mass ratio inspirals (e.g., Berti et al. 2006; Barack & Cutler 2007; Babak et al. 2017; Moore et al. 2017), merging black holes with masses between 10^4–10^7 $M_\odot$ (e.g., Klein et al. 2016; Bellovary et al. 2019), and cosmological GW backgrounds (e.g., Bartolo et al. 2016; Caprini et al. 2016; Caldwell et al. 2019). For sources which have signals buried by the Galactic DWD population, the foreground must be carefully analyzed and subtracted (Adams & Cornish 2014; Cornish 2020; Littenberg et al. 2020; Boileau et al. 2021). The number of resolved DWDs and the height of the unresolved DWD foreground are a direct consequence of the number of DWD progenitors which form and evolve over the Milky Way's history.

While the binary fraction remains approximately constant across a large metallicity range ($-1.5 \leq$ [Fe/H] < 0.5) for wide binaries, close OB stars, and the stellar Initial Mass Function (IMF) (Moe & Di Stefano 2017; Moe et al. 2019), the binary fraction for solar-type star systems with orbital period $P_{\rm orb} \leq 10^4$ days (separation $a \leq 10$ AU) shows a strong anti-correlation with metallicity (e.g. Badenes et al. 2018; Moe et al. 2019; Mazzola et al. 2020; Price-Whelan et al. 2020). Because close DWDs are the remnants of close, solar-type binary stars, this anti-correlation plays an important role in the formation, evolution, and characteristics of the DWD population that LISA will observe.

To date, population synthesis studies of the Galactic population of close DWDs have either assumed a 100% binary fraction or a 50% binary fraction, such that for every three stars formed, two reside in a binary system (Nelemans et al. 2001; Yu & Jeffery 2013; Korol et al. 2017; Lamberts et al. 2019). In this study, we investigate the effects of a metallicity-dependent binary fraction on the formation and evolution of DWDs. To this end, we create synthetic present-day Milky Way-like galaxies of DWDs and specifically select systems with GW signals that may be observable by the space-based detector LISA. Throughout, we make comparisons between the standard assumption of a constant 50% initial binary fraction (hereafter model F50) and one with a metallicity-dependent binary fraction (hereafter model FZ).

In Section 2 we discuss our binary evolution assumptions used in simulating DWD populations and detail the process to produce present-day synthetic Milky-Way-like galaxies. In Section 3 we review the derivation of LISA detectability for circular DWD populations at mHz frequencies. In Section 4 we detail results showing how a metallicity-dependent binary fraction affects the formation and evolution of DWD populations assuming a fiducial set of binary evolution assumptions. In Section 5 we detail the metallicity dependence of the LISA DWD foreground and resolved population. Finally, we repeat our analysis for three sets of binary evolution assumptions to show a robust reduction of the size of the Galactic DWD foreground in LISA for populations simulated with a metallicity-dependent binary fraction in Section 6 and conclude in Section 7.

2. SIMULATING A GALACTIC DWD POPULATION

In this section we describe the setup of our DWD simulations using the binary population synthesis suite `COSMIC`, and the process to scale these simulations to create Milky Way-like galaxies using the star formation history of galaxy **m12i** in the Latte suite of the FIRE-2 simulations (Wetzel et al. 2016; Hopkins et al. 2018) and stellar positions assigned according to the the Ananke framework (Sanderson et al. 2020).

2.1. *Binary population models*

We simulate the evolution of DWD progenitor populations using COSMIC[1], an open-source Python-based rapid binary population synthesis suite which employs single and binary star evolution using SSE/BSE (Hurley et al. 2000, 2002). Several modifications have been added to COSMIC which incorporate updates for massive star evolution and binary interactions. For a detailed description of these modifications see Breivik et al. (2020b). COSMIC has been used in several studies to examine the effects of binary evolution on binary populations from blue stragglers (Leiner & Geller 2021) and heartbeat stars (Jayasinghe et al. 2021), to white dwarf populations (Kremer et al. 2017; Breivik et al. 2018; Kilic et al. 2021), to merging compact object populations in isolated binaries (Zevin et al. 2020a,b, 2021; Wong et al. 2021; Mandhai et al. 2021) and in dynamical environments around super-massive black holes (Stephan et al. 2019; Wang et al. 2021).

COSMIC is especially useful for efficient generation of large populations of compact binaries. Instead of choosing a fixed number of binary stars for each simulation, COSMIC iteratively simulates populations until parameter distributions of the binary population converge to a stable shape as more binaries are added. This process is quantified through the *match* parameter inspired by matched filtering techniques (e.g. Eq. 6 of Chatzioannou et al. 2017) defined as

$$match = \frac{\sum_{k=1}^{N} P_{k,i} P_{k,i+1}}{\sqrt{\sum_{k=1}^{N} P_{k,i} P_{k,i} \sum_{k=1}^{N} P_{k,i+1} P_{k,i+1}}}, \qquad (1)$$

where $P_{k,i}$ represents the height of bin k on the ith iteration (Breivik et al. 2020b). In this study, we simulate binaries until $\log_{10}(1 - match) \leq -5$ for the masses and orbital periods of each DWD population at the formation of the second WD. Since all DWD progenitor binaries simulated with COSMIC are circularized through mass transfer or tides before the second WD forms (e.g. Marsh et al. 2004; Gokhale et al. 2007; Sepinsky & Kalogera 2014; Kremer et al. 2015), we do not consider convergence of DWD eccentricities.

The masses and orbital periods at the formation of the second-formed WD span a wide range depending on the WD binary component types, thus we consider four DWD combinations: two helium WDs (He + He), a carbon-oxygen WD orbiting a helium WD (CO + He), two carbon-oxygen WDs (CO + CO), and an oxygen-neon orbiting a helium, carbon-oxygen, or oxygen-neon WD (ONe + X). For each DWD type we simulate a grid of 15 metallicities spaced uniformly in $\log_{10}(Z)$ between $Z = 10^{-4}$ to 0.03, to account for the limits of the Hurley et al. (2000) stellar evolution tracks employed in COSMIC. This results in a total of 60 populations across all DWD types and metallicities. The output of COSMIC contains information limited to intrinsic binary properties like mass and orbital period. External parameters like Galactic position and orientation are assigned in a post-processing scheme which uses metallicity-dependent positions and ages from the Ananke framework of galaxy **m12i** from the Latte Suite of the FIRE-2 simulations (see Section 2.3 for details).

We assume that the Zero Age Main Sequence (ZAMS) masses, orbital periods and eccentricities for each binary are independently distributed. We choose primary masses following Kroupa (2001), a flat mass ratio distribution (Mazeh et al. 1992; Goldberg & Mazeh 1994), a log-uniform period distribution following Opik's Law, and a uniform eccentricity distribution following Geller et al. (2019). We initialize all binaries with the same evolution time of 13.7 Gyr to capture all potential evolution within a Hubble time. We assume a 100% binary fraction in our COSMIC simulations to reduce computation time and scale the simulations to models which assume a constant 50% binary fraction (model F50) or a metallicity-dependent binary fraction (model FZ) in a post-processing scheme.

Since we are primarily interested in the effects of a metallicity-dependent binary fraction, we use a single set of assumptions for binary interactions. Our choices follow the COSMIC defaults described in Breivik et al. (2020b) except for the treatment of Roche-lobe overflow (RLO). The stability of RLO mass transfer is determined using critical mass ratios resulting from radius-mass exponents (Webbink 1985; Hurley et al. 2002), where the critical mass ratio is defined as the ratio of the donor to accretor mass. We assume critical mass ratios following Claeys et al. (2014) which reduce the standard critical mass ratio assumptions from Hurley et al. (2002) for main sequence (MS) donors by $\sim 50\%$ from 3 to 1.6 based on the models of de Mink et al. (2007) and treat WD accretors separately following the models of Soberman et al. (1997). We increase the mass loss rate from the donor following Equation 11 of Claeys et al. (2014). The amount of mass lost during RLO from the donor is limited by the overflow factor of the donor radius to its Roche radius following Hurley et al. (2002). The amount of mass accepted by the accretor is limited to 10 times the accretor's mass divided by the accretor's thermal timescale. Finally, for RLO mass loss which becomes unstable and leads to common envelope evolu-

[1] https://cosmic-popsynth.github.io

tion (CEE) we assume that the donor's binding energy is calculated according to the fits detailed in Appendix B of Claeys et al. (2014) and that orbital energy is deposited with 100% efficiency into unbinding the common envelope ($\alpha = 1$).

2.2. *Metallicity-dependent binary fraction*

We fit the results presented in Moe et al. (2019) using linear regression to obtain a piecewise relation between the metallicity, [Fe/H] and binary fraction f_b as

$$f_\mathrm{b} = \begin{cases} -0.0648 \cdot [\mathrm{Fe/H}] + 0.3356, & [\mathrm{Fe/H}] \leq -1.0 \\ -0.1977 \cdot [\mathrm{Fe/H}] + 0.2025, & [\mathrm{Fe/H}] > -1.0 \end{cases} \tag{2}$$

We convert between [Fe/H] and metallicity Z, assuming all stars have solar abundance such that

$$[\mathrm{Fe/H}] = \log_{10}\left(\frac{\mathrm{Z}}{\mathrm{Z}_\odot}\right), \tag{3}$$

where we assume $Z_\odot = 0.02$.

2.3. *A metallicity-dependent SFH: Convolving with the FIRE-2 models*

To create Milky Way-like galaxies which integrate the metallicity-dependent binary fraction, we use the metallicity-dependent ages and positions of galaxy **m12i** from the "Latte" suite of the FIRE-2 simulations (Hopkins 2015; Wetzel et al. 2016; Hopkins et al. 2018) to create synthetic, Milky Way-like DWD populations.

The **m12i** galaxy provides particle mass resolution of 7070 $\mathrm{M}_\odot$ per star particle. Each star particle has an associated metallicity, position, and age, which is combined with the output of `COSMIC` to assign DWDs to each star particle by matching its metallicity to our `COSMIC` metallicity grid. The positions of each DWD are assigned using the Ananke framework since multiple DWD binaries can form within a single star particle. Specifically, we use an epanechnikov kernel where the kernel size is inversely proportional to the local density to assign the radial component of spherically symmetric offsets from the center of each star particle following Sanderson et al. (2020).

The metallicity-dependent binary fraction is shown in black in Figure 1 along with the mass in star particles from galaxy **m12i**, shown in red, as a function of our metallicity grid. The binary fraction, f_b, drops drastically across metallicity while the mass formed in **m12i** increases significantly. These two opposing trends compete throughout this study along with the impact of metallicity on single star evolution to form the final numerical distribution of systems in our DWD populations.

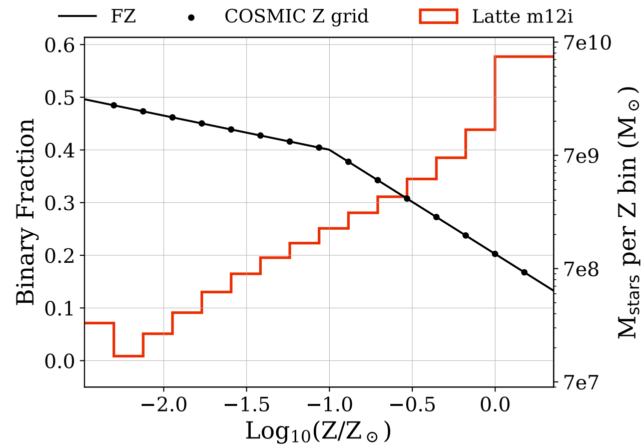

Figure 1. The metallicity-dependent binary fraction for close solar-type binaries with P < 10^4 days (black) plotted against the logarithm of $\mathrm{Z/Z_\odot}$, with scatter points denoting the location of the metallicity grid used in our `COSMIC` simulations. The secondary axis shows the amount of mass in stars formed within each metallicity bin from galaxy **m12i** of the "Latte" suite in the FIRE-2 simulations as a red histogram. The amount of stellar mass formed with super-solar metallicities dominates the distribution. Note that the primary axis shows $f_\mathrm{b}(Z)$ in linear scale, and the secondary axis shows amount of mass formed in log-scale. The opposing trends of these two distributions compete throughout this study.

Since our `COSMIC` simulations assume a binary fraction of $f_\mathrm{b} = 1$, we scale the amount of mass sampled at ZAMS required to produce our `COSMIC`-generated population of DWDs ($M_\mathrm{b,ZAMS}$) to the proper amount of mass sampled in single and binary stars ($M_\mathrm{ZAMS,sim}$) for each binary fraction and model. We do this by sampling single stars and primary masses of binary stars from the Kroupa (2001) IMF and sampling secondary masses of the binary stars from a uniform mass distribution, where the number of binaries is determined by the binary fraction model (F50 or FZ). From this sample, we obtain the ratio of mass in single stars to the mass in binary stars as a function of the binary fraction, $R(f_\mathrm{b})$. For model F50, the ratio is a constant $R(f_\mathrm{b}) = 0.64$. For model FZ, the ratio increases from 0.68 at low metallicities to 3.17 at solar metallicity indicating less mass in binaries relative to single stars. The total amount of ZAMS mass in single and binary stars is then $M_\mathrm{ZAMS,sim} = M_\mathrm{b,ZAMS}(1 + R(f_\mathrm{b}))$.

Once we determine the total ZAMS mass required to produce our simulated population for a given metallicity, the number of DWDs formed per unit solar mass at metallicity Z_i is

$$n_\mathrm{DWD}(Z_i) = \frac{N_\mathrm{DWD,sim}(Z_i)}{M_\mathrm{ZAMS,sim}(Z_i)}. \tag{4}$$

The number of DWD's per **m12i** star particle at metallicity Z_i is then

$$N_{\rm DWD,\star}(Z_i) = n_{\rm DWD}(Z_i)\, M_\star, \tag{5}$$

where $M_\star = 7070\, M_\odot$ is the mass per **m12i** star particle. Since $N_{\rm DWD,\star}(Z_i)$ is not an integer, we treat the decimal component as the probability that the star particle contains an extra DWD in addition to the integer number. For each star particle, we sample with replacement $N_{\rm DWD,\star}(Z_i)$ DWDs from the corresponding simulated `COSMIC` population at that metallicity and assign the ZAMS birth time of each DWD to the formation time of the star particle. For most DWD types there is more than one DWD binary system assigned to each **m12i** star particle.

If the DWD formation time is less than the age of the star particle, we evolve the DWD over the remaining time between its formation and star particle age, $t_{\rm evol}$, to produce the present-day population. Once a DWD is formed, we assume that the binary evolves only due to the emission of GWs. Due to tidal effects and mass transfer between their progenitor binaries, all DWDs in our simulations are circular, thus eccentricity does not need to be considered. The orbital evolution over the time $t_{\rm evol}$ is then simply defined according to Peters (1964) as

$$a_f = (a_i - 4\beta t_{\rm evol})^{1/4}, \tag{6}$$

where a_i is the DWD separation at formation, and

$$\beta = \frac{64G^3}{5c^5} M_1 M_2 (M_1 + M_2) \tag{7}$$

is constant throughout DWD evolution (Peters 1964).

We discard any DWDs for which the sum of their ZAMS birth time, given by the star particle formation time, and DWD formation time is larger than the age of the star particle since the system will not have evolved long enough to become a DWD at present. We further discard any DWDs for which the lower mass WD overflows it's Roche lobe before present day, because the outcomes of these interactions are highly uncertain and their treatment is outside the scope of this work (e.g., Shen 2015; Kremer et al. 2017). **We also note that stably accreting WD binaries are unlikely to contribute appreciably to the Galactic DWD foreground due to their small mass ratios at frequencies below** 1 mHz **(Breivik et al. 2018).** The separation at which the lower mass WD overflows its Roche Lobe is defined as

$$a_{{\rm RLO},\ell} = R_\ell \frac{0.6 q_\ell^{2/3} + \ln\left(1 + q_\ell^{1/3}\right)}{0.49 q_\ell^{2/3}} \tag{8}$$

where R_ℓ is the radius of the lower mass WD and $q_\ell = M_\ell / M_h$ is the ratio of the lower- to higher-mass WD components. (Eggleton 1983). We define the radius of a WD following Tout et al. (1997); Hurley et al. (2000) as

$$R_{\rm WD} = \max\left(R_{\rm NS}, 0.0115\sqrt{\left(\frac{M_{\rm Ch}}{M}\right)^{2/3} - \left(\frac{M}{M_{\rm Ch}}\right)^{2/3}}\right) \tag{9}$$

where $R_{\rm NS} = 1.4 \cdot 10^{-5}\ {\rm R}_\odot$ is the radius of a neutron star, $M_{\rm Ch} = 1.44\ {\rm M}_\odot$ is the Chandrasekhar limit for the mass of a stable WD, and M is the mass of the WD in solar masses.

For the non-discarded systems, we log the present-day separations from which the present-day orbital frequency $f_{\rm orb}$ can be found using Kepler's third law. The GW frequency is then $f_{\rm GW} = 2 f_{\rm orb}$.

3. LISA DETECTABILITY

We use `LEGWORK`[2] (Wagg et al. 2021) to determine the detectability of our simulated DWD populations for sources with GW frequencies $f_{\rm GW} > 10^{-4}$ Hz. `LEGWORK` calculates the position-, orientation-, and angle-averaged signal to noise ratio (SNR) for inspiraling GW sources closely following the derivations of Flanagan & Hughes (1998) and using the LISA noise power spectral density (PSD) of Robson et al. (2019).

To lowest order in the post-Newtonian expansion, the frequency evolution of circular orbits for quadrupole GW emission is defined as

$$\dot{f}_n = \frac{48n}{5\pi} \frac{(G\mathcal{M}_c)^{5/3}}{c^5} (2\pi f_{\rm orb})^{11/3}. \tag{10}$$

We classify DWDs as evolving, or "chirping", when $\dot{f}_n \geq 1/t_{\rm obs}^2$. For evolving sources, the SNR is

$$\langle\rho\rangle^2_{\rm circ,evol} = \int_{f_0}^{f_1} df\, \frac{h_c^2}{f^2 S_n(f)} \tag{11}$$

where h_c is the characteristic strain of the system, $S_n(f)$ is the LISA sensitivity curve of Robson et al. (2019), and the frequency limits are determined by the orbital evolution over the observation time, $T_{\rm obs} = 4$ yr. The characteristic strain for circular orbits is

$$h_c^2 = \frac{2^{2/3}}{3\pi^{4/3}} \frac{(G\mathcal{M}_c)^{5/3}}{c^3 D_L^2} \frac{1}{f_{\rm orb}^{1/3}}, \tag{12}$$

where $\mathcal{M}_c = (M_1 M_2)^{3/5} / (M_1 + M_2)^{1/5}$ is the system's chirp mass, and D_L is the systems luminosity distance

[2] https://legwork.readthedocs.io

which we assume to be the distance of each simulated DWD to the Sun.

For stationary sources, the SNR is modified due to the lack of observable orbital evolution as

$$\rho^2_{\rm circ,stat} = \frac{h_2^2 T_{\rm obs}}{4S_n(f_2)} \tag{13}$$

with the observation time $T_{\rm obs}$. Here, h_2 is strain amplitude of the source for the second orbital frequency harmonic,

$$h_2^2 = \frac{2^{22/3}}{5}\frac{(G\mathcal{M}_c)^{10/3}}{c^8 D_L^2}(\pi f_{\rm orb})^{4/3} \tag{14}$$

and is connected to the characteristic strain as

$$h_2^2 = \frac{\dot{f}_2}{f_{\rm orb}^2} h_c^2 \tag{15}$$

The amplitude spectral density for a stationary system is finally defined as $ASD = h_2\sqrt{T_{\rm obs}}$, such that the SNR for stationary source is simply, $\rho \sim ASD/S_n$.

The Galactic foreground included in the Robson et al. (2019) LISA noise curve was generated using a different binary evolution code and set of model assumptions for DWD formation and evolution (Toonen et al. 2012; Korol et al. 2017). Thus, we use the detector curve only and generate an approximate foreground from each of our populations as follows. Instead of performing a full source subtraction algorithm (e.g. Littenberg et al. 2020), which is out of the scope of this work, we calculate the PSD of the Galactic DWD population with a frequency resolution set by the LISA mission time as $1/T_{\rm obs} \sim 1/4\,{\rm yr}^{-1} \sim 8\times10^{-9}$ Hz. We then approximate the foreground as the running median of the PSD with a boxcar window with a width of 10^3 frequency bins similar to Benacquista & Holley-Bockelmann (2006). The Galactic DWD PSD is truncated near 10 mHz for both of our models because we remove all DWDs which experience Roche-lobe overflow. In order to smooth the effect of this truncation in our foreground, we fit each running median with fourth-order polynomials for GW frequencies up to 1 mHz, thus allowing an approximation of the foreground PSD for higher frequencies. These fits are listed in Table 1 where the polynomial is described as

$$\log_{10}(\text{confusion fit/Hz}) = \mathrm{a}\,\mathrm{x}^4 + \mathrm{b}\,\mathrm{x}^3 + \mathrm{c}\,\mathrm{x}^2 + \mathrm{d}\,\mathrm{x} + \mathrm{e} \tag{16}$$

and $x = \log_{10}(f_{\rm GW}/{\rm Hz})$. We add the fitted polynomial of the PSD's running median to the LISA noise PSD to obtain a sensitivity curve for each model.

model	a	b	c	d	e
F50	-223.5	-189.8	-76.8	-14.0	-1.0
FZ	-558.5	-575.4	-243.1	-45.8	-3.2

Table 1. Polynomial fitting coefficients for the confusion foreground fit of Equation 16 for each binary fraction model.

4. METALLICITY EFFECTS ON THE FORMATION AND EVOLUTION OF DWDS

4.1. *DWD types and their formation channels*

As discussed in Section 2.1, we consider four DWD sub-types, which each contribute differently to LISA's GW signals: He + He, CO + He, CO + CO, and ONe + X. Each sub-type has a unique distribution in their formation times, initial masses, radii, and orbital periods stemming from variations in their evolution channels and their formation efficiency. Here we describe the general formation scenarios and population properties of Galactic close DWDs which may be observable by LISA.

He WDs are unable to form through single star evolution within the lifetime of the Milky Way. Instead, they originate through interactions in close binary systems or binaries with large eccentricities. Because of this, He WDs are able to form with low component masses on order $\sim 0.1{\rm M}_\odot$, with the majority of He WDs in our simulations having masses between 0.2-0.5 ${\rm M}_\odot$. He + He DWDs form through evolution of close binary systems, during which their envelopes are both stripped through RLO and CE phase interactions before Helium ignition occurs. The two progenitor stars generally have masses $\lesssim 3M_\odot$ which is lower than the progenitors of other DWD types. Our simulated He + He DWDs have an approximately constant distribution of formation times $\gtrsim$ 2.5 Gyr. Lastly, since the ZAMS separations are skewed towards shorter values, we also see that the resulting DWD separations are smaller on average than that of other DWD types.

A CO WD forms when a star is able to begin the helium burning process before its envelope is stripped. Thus to form a CO + He DWD, RLO and CE stages occur after one component experiences core helium burning, but before the other component can. Most close CO + He DWDs form in approximately 2 Gyr after ZAMS and with very short periods because the He WD is formed through the ejection of a common envelope which greatly reduces the orbital separation. Because of these short formation separations, many CO + He DWDs merge before the present day. Due to their asymmetric mass distributions, they have lower chirp masses, but their shorter periods make them important candi-

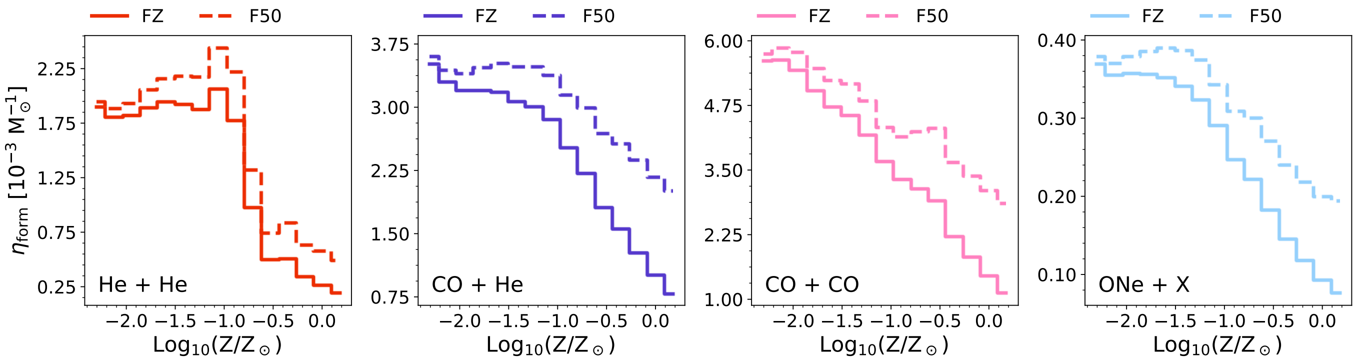

Figure 2. The DWD formation efficiency vs metallicity of DWD populations simulated with `COSMIC`. Each panel shows the formation efficiency for a given DWD type. The solid lines indicate the formation efficiency for model FZ which incorporates a metallicity-dependent binary fraction. The dashed lines indicate the formation efficiency for model F50, which assumes a constant binary fraction of 50%. The DWD formation efficiency drops by a factor of $4-5$ for model FZ and a factor of 2-5 for model F50. See Section 4.2 for a careful description of the trends for each DWD type.

dates for LISA detection.

To prevent the two stars' envelopes from being stripped before helium ignition, CO + CO DWDs typically form from progenitors in wider orbits, and the two components may have little to no interaction during their evolution from ZAMS to DWD. CO DWDs thus have a distribution in progenitor separation that extends to larger values than for other DWD types. Most need >0.3 Gyr to form. These systems have component WD masses between 0.35–1.0 $M_\odot$ and make up the majority of the DWD population.

ONe WDs are rare and typically form from massive progenitor stars which evolve through the asymptotic giant branch (AGB) phase, thus resulting in a higher mass WD. All ONe WDs in our `COSMIC` populations, e.g., have progenitor ZAMS masses above $4\,M_\odot$, and the resulting ONe WDs have a relatively flat distribution of masses from $1.05\,M_\odot$ up to the Chandrasekkhar limit of $1.4\,M_\odot$. Because an ONe WD can have a companion of any other WD type in our study, there is a spread in their distributions for separation, secondary mass, final orbital period, and formation time. In general, however, these systems result from wider separations to allow for the evolution of the ONe component without merging, e.g. all initial separations in our `COSMIC` populations have separations $\gtrsim 1.5\,R_\odot$. ONe + X DWDs can form on short timescales, as low as 30 Myr for the majority of high-metallicity systems.

4.2. *Metallicity-dependent trends in the formation efficiency of DWDs*

The number of DWDs formed per unit solar mass of ZAMS star formation, or DWD formation efficiency $\eta_{\rm form}(Z)$), varies with metallicity. Consequently, a metallicity-dependent binary fraction further impacts the efficiency of DWD formation within the Galaxy. Figure 2 shows the DWD formation efficiency as a function of metallicity for each DWD type and for each of our binary fraction models. In general, the formation efficiency decreases with increasing metallicity. This effect is exaggerated for model FZ which assumes a binary fraction which also decreases with increasing metallicity.

For He + He DWDs, the sudden drop in formation efficiency near $\log(Z/Z_\odot) = -1.0$, is generally caused by the timescale for which the initially more massive star in the DWD progenitor overflows it's Roche lobe. At lower metallicities, donors tend to fill their Roche lobes while they are still on the main sequence and the mass transfer remains stable. This is because, in our `COSMIC` models lower metallicity stars evolve faster than high-metallicity stars and have larger radii near the end of the MS. At higher metallicities, mass transfer is initiated when the donor has left the main sequence and the binary enters a common envelope evolution. The ZAMS orbital period leads to different specific evolutionary channels. For short-period systems with periods below 10 days, this leads to a stellar merger due to insufficient orbital energy to eject the envelope. Stellar mergers continue to dominate the evolutionary pathways of systems with intermediate orbital periods ($1 < \log_{10}(P_{\rm orb}/{\rm day}) < 2.5$). However, an additional growing number of merging systems arises with one WD component and one stellar companion, and systems which don't interact at all and thus do not form a He + He DWD. The distinction between the various scenarios in this intermediate orbital period range depends on the combination of their ZAMS masses and orbital periods. Finally, at wider initial periods $\log_{10}(\rm P) > 2.5$, the decrease in formation efficiency is dominated by systems which never interact and thus do not form a DWD before the present day.

For short-period CO + He DWD progenitor binaries

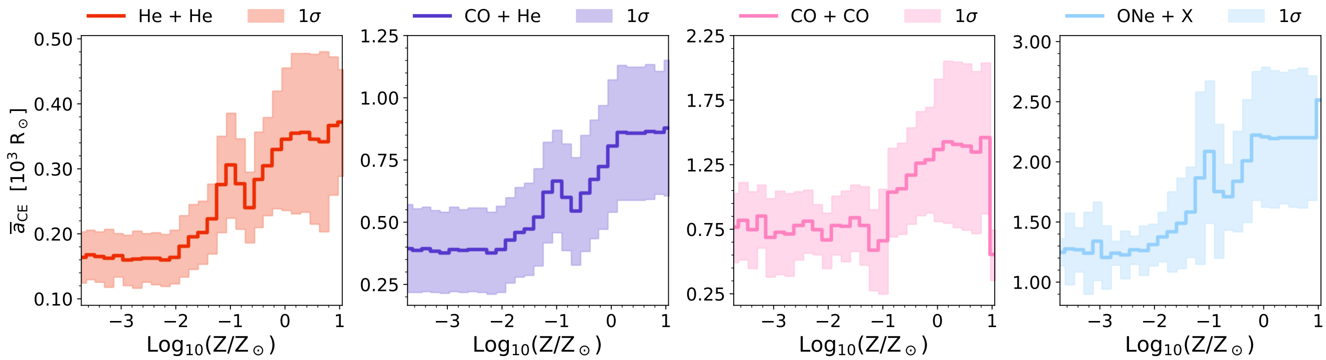

Figure 3. Average interaction separation, $\bar{a}_{\rm CE}$ of progenitors of close DWDs across metallicity for each DWD type from model FZ. Solid lines show the average separation at the first RLO for binaries in each metallicity bin. The shaded regions show the 1σ spread around the mean within each metallicity bin. The average interaction separation increases with metallicity for every DWD type. The positive trend in the average interaction separation is a direct consequence of larger envelope masses of higher-metallicity donors which are less evolved than their lower-metallicity counterparts. The sharp drop of the CO + CO average at the highest-metallicity bin is due to binning effects of the figure: it only contains 115 systems, of which the majority stem from a single low-separation system which was sampled 94 times times during the simulation.

with orbital periods below $\sim$ 30 days, the only channel for mergers before DWD formation is during a CE evolution. This channel is similar to the stellar merger channel for He + He DWDs, but due to higher-mass progenitors the CE evolution results in the binary component with a higher mass becoming a CO WD. At higher metallicities, the CO WD merges with its companion. Higher-metallicity progenitors have a larger fraction of their mass in the convective envelope when compared to lower-metallicity stars of the same mass (Amard, L. et al. 2019; Amard & Matt 2020) Thus a CE phase with a higher-metallicity progenitor requires more orbital energy to eject the common envelope, causing a larger amount of orbital shrinking which results in a merger later in its binary evolution.

For CO + He DWD progenitor systems with intermediate orbital periods ($1.5 \leq \log_{10}(P_{\rm orb}/{\rm day}) < 2.5$) the mechanisms which impact formation efficiency are complex. The dominant way to lose CO + He DWDs is stellar mergers that occur during the second CE phase. For lower-metallicity systems, the second CE is successful, while the opposite is true for higher-metallicity systems. This is again because the envelope mass of the CE evolution donor at higher metallicity is larger than it would be at lower metallicity and thus requires more orbital energy to eject in the CE phase. This leads to shorter post-CE orbital periods after the first CE phase and hence mergers during the second phase.

If a lower-metallicity system forms a CO + He DWD and a higher-metallicity system does not, this is because the initially more massive binary component initiates a CE while on the giant branch (GB) instead of the asymptotic giant branch (AGB). This instead leaves behind a He WD with a stellar companion, which is the dominating scenario that restricts formation efficiency. There are a few edge cases where either a He + He DWD is formed instead, or when a CO WD and a stellar companion is formed and there has been very nearly but not quite enough time for a CO + He DWD to form.

Long-period binaries with $\log_{10}(P_{\rm orb}/{\rm day}) > 2.5$ also display complex scenarios that hinder CO + He DWD formation. In near-equal contributions, our `COSMIC` simulations produce either stellar mergers or stable non-DWD binaries at the end of the Hubble time. At these orbital periods, stellar mergers always occur with a CE phase between a stellar companion and a CO or He WD. Similar to binaries with shorter orbital periods, the mergers occur because of increased CE donor envelope masses at higher metallicities. A subdominant channel of stable He + He DWDs can also occur when a high-metallicity primary overflows it's Roche lobe while still on the GB and thus forms a He WD.

The decrease in the CO + CO DWD formation efficiency with increasing metallicity stems from different evolutionary channels which arise at the ZAMS orbital period boundary of $\log_{10}(P_{\rm orb}/{\rm day}) \simeq 3$. We find that for binaries with orbital periods below this boundary, the most common way that CO + CO DWDs form at lower metallicities but not at higher metallicities is through stellar mergers during a CE phase with a donor that is still on the GB. For lower-metallicity binaries, which evolve on faster timescales, the primaries enter CE evolution while on the AGB instead and the binary is able to survive. For binaries with orbital periods above the boundary, the vast majority of systems with wide initial orbits end up as stable binaries. The systems which don't form a CO DWD at high metallicity do so because one or both of the binary components initiate a

CE phase while still on the GB thus producing a CO + He or He + He DWD.

The strongest effect which hinders formations of higher-metallicity ONe + X DWDs is the strength of metallicity-dependent stellar winds assumed in our model (Vink et al. 2001). The strength of line-driven winds varies more strongly for the more massive ($\geq 5\,\mathrm{M}_{\odot}$) progenitors of ONe WDs relative to the other lower mass WD progenitors. At higher metallicities, ONe WD progenitors can lose enough mass through winds such that they don't ignite their CO cores and thus leave behind a CO WD. Conversely, the lower-metallicity progenitors retain enough mass to cause carbon ignition and leave behind an ONe WD.

4.3. *Metallicity trends in DWD progenitor common envelope separation*

All systems that end up radiating GWs in the LISA band have undergone at least one phase of CE evolution. For systems which experience a stable RLO mass transfer in the first interaction, the CE phase plays a key role in shrinking systems with initially wide separations to bring them into the LISA band.

Figure 3 shows the average separation at the first instance of CE evolution, a_{CE} of all DWD progenitors that result in systems orbiting in the LISA frequency band at present day, as a function of metallicity for each DWD type. The solid lines denote the average value, and the 1σ variance is shown in the surrounding shading. The average CE separation increases in general across metallicity. Higher-metallicity binaries will interact earlier in the binary's lifetime than a lower-metallicity binary of equal separation due to their relatively larger maximum radii. Since higher-metallicity binaries are also more likely to merge during CE interactions because of their relatively more massive donor envelopes, the DWDs which survive and eventually orbit in the LISA band originate from systems with higher interaction separations which allow their orbits to shrink significantly during CE phases without merging. This regulation plays a key role in smearing out any observable effects of a metallicity-dependent binary fraction in the population of DWDs observable by LISA.

Note that the average CE separation is close to the qualitative limit for close binaries of $P_{\mathrm{orb}} \gtrsim 10^{4}$ day for the CO + CO and ONe + X binaries. We investigated the fraction of close DWD progenitors which formed with orbital periods above this range for each DWD type. For the He + He DWDs, less than 10% of all progenitors, regardless of metallicity originate in wide orbits. For CO + He population, the percentage increases from 10–15% from low to high metallicities, and for the more massive CO + CO and ONe + X DWDs, the percentages increase from 15–25% and 20–40% respectively. This suggests that our application of the close binary fraction may not be valid over the entire range of the DWD progenitor population. However, since the relative sizes of CO + CO and ONe + X are small compared to the He + He and CO + He populations, we leave a further investigation of these effects to a future study.

5. METALLICITY DEPENDENCE OF THE LISA DWD POPULATION

While metallicity impacts the intrinsic properties of our simulated DWD populations as described in Sections 4.2 and 4.3, when we consider the present-day Galactic close DWDs we find that the population detectable by LISA changes only numerically. The number of DWDs in the LISA frequency band decreases by $\sim 50\%$ when comparing model F50 to model FZ.

Figure 4 shows the number of DWDs orbiting with frequencies $f_{\mathrm{GW}} > 0.1\,\mathrm{mHz}$ against metallicity for each DWD type. The solid lines show DWDs from model FZ, and the dashed lines show DWDs from model F50. The He + CO, CO + CO, and ONe + X populations each have strong peaks in the number of DWDs near solar metallicity at which the majority of star formation in galaxy **m12i** occurs. The largest contribution to the population comes from metallicities above $\sim 0.01\mathrm{Z}_{\odot}$. The discrepancy between the two binary fraction models is also the most significant above this threshold. When creating our DWD populations the DWD formation efficiency, number of **m12i** star particles, and binary fraction all compete. The amount of stars formed in **m12i** at higher metallicity values overwhelms the drop in DWD formation efficiency by multiple orders of magnitude, so this effect dominates when determining the number of stars initially sampled in the population for f_{b}.

There are two peaks in the distribution of He + He DWDs. This occurs because near $Z \simeq 0.1Z_{\odot}$, the DWD formation efficiency transitions from near constant values to a sharp decrease (see Figure 2). However, for a drop in the formation efficiency by a factor of of $\sim$ six, the amount of star formation in galaxy **m12i** increases by more than an order of magnitude for super-solar metallicities. Above $Z = Z_{\odot}$ this overcompensates for the efficiency drop, producing the second peak.

The reduced number of DWDs in model FZ relative to model F50 is also apparent in the GW PSD LISA will observe. We show the GW PSD of each model, as well as the confusion estimate, in Figure 5. While model F50 (dark blue) and model FZ (light blue) produce several thousand large spikes in the PSD across

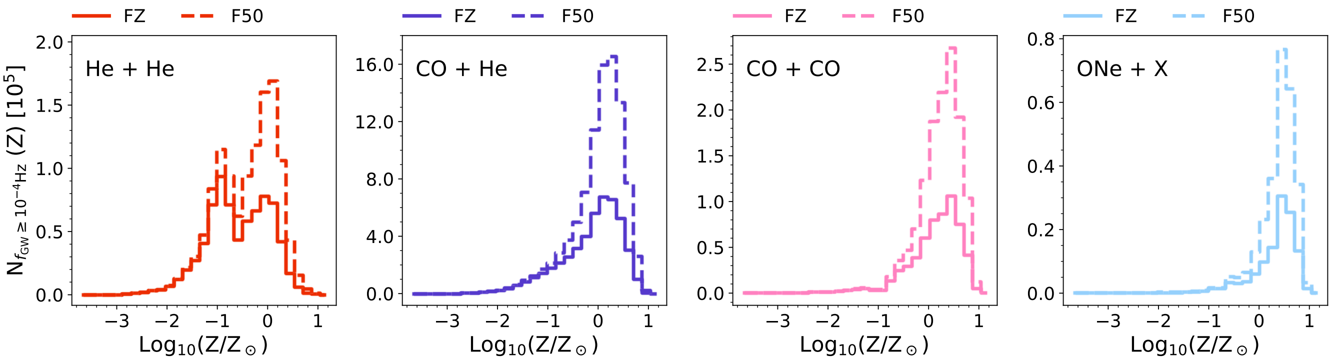

Figure 4. The number of LISA-band systems formed for each DWD type as a function of the base-10 logarithm of metallicity, normalized to solar value. The solid line shows the FZ population with a metallicity-dependent binary fraction incorporated, and the dashed line shows the F50 population for a standard binary fraction of 0.5. The LISA population of DWDs is dominated by stars with super-solar metallicities. This is true even for model FZ, which drops off significantly for higher metallicities, because of the large number of stars formed in **m12i** beyond Z$\simeq$Z$_\odot$. There is a double peak in the He + He population; the first peak is caused by the sharp drop in formation efficiency past Z$\simeq 0.1 Z_\odot$ which is then greatly overcompensated for by the amount of star formation at higher metallicities which forms the second peak.

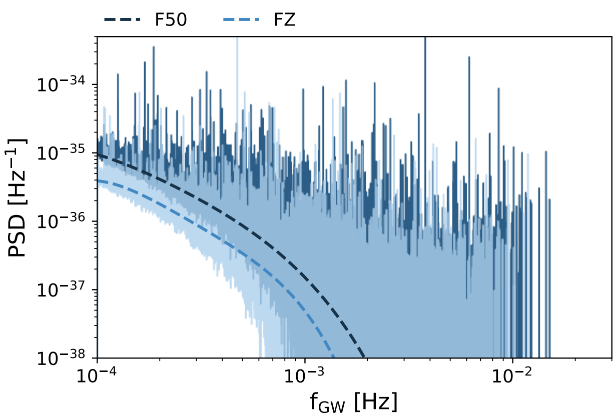

Figure 5. The PSD of the entire Galactic DWD GW foreground, summed over all metallicities and DWD types vs GW frequency for models FZ and F50. The vertical lines show the PSD where model F50 is shown in dark blue and model FZ is shown in light blue. The dashed lines show fits to the rolling boxcar median of width 1000 bins for each PSD (see 3 for a discussion). A metallicity-dependent binary fraction (model FZ) yields fewer DWDs across all frequencies than a 50% binary fraction (model F50) by roughly a factor of 2. This produces a lower GW confusion foreground for frequencies with $f_{GW} \leq\sim 10^{-3}$ Hz.

LISA's frequency band, the overall foreground height, including the confusion, is larger for model F50. This is a direct consequence of the overall reduction in the size of the close DWD population in model FZ.

Similar to previous studies, we find that LISA will be able to resolve several thousand DWDs. Figure 6 shows the amplitude spectral density vs GW frequency of the resolved systems with SNR $>$ 7 for each DWD type, where the top and bottom rows show results for models FZ and F50 respectively. For comparison, we also show the LISA sensitivity curve, including the modeled confusion foreground from each population in black, and the the entire population for each model in grey. Apart from each DWD type having a different abundance of resolved systems, the population-wide characteristics remain unchanged between the two binary fraction models. The populations containing at least one He WD occupy the lower-ASD, higher-GW frequency region of parameter space compared to the total population, with CO + He DWDs having larger ASDs than the He + He DWD population. Conversely, DWD types without a He WD component tend to occupy the higher-ASD, lower-GW frequency region of parameter space. This difference is largely due to the formation scenario of DWDs containing a He WD, which form from the ejection of a common envelope created by the He WD progenitor. These lower mass progenitors overflow their Roche lobes at closer separations relative to the higher mass progenitors (e.g. Figure 3) and thus also produce closer DWDs. While the distance to any one DWD strongly influences its ASD, DWD populations without a He WD component have, on average, higher ASDs due to their more massive WD components.

We note that while the height of the confusion foreground and the number of DWDs radiating GWs with $f_{GW} > 10^{-4}$ Hz is reduced by a factor of 2 for model FZ relative to model F50, the number of resolved sources is not reduced to an equal degree. This is because in the absence of less competing GW signals from DWDs in the LISA frequency band, more DWDs can be individually resolved. Between models FZ and F50, the number of resolvable systems with SNR $>$ 7 over all DWD types decreases by only $\sim$ 14%.

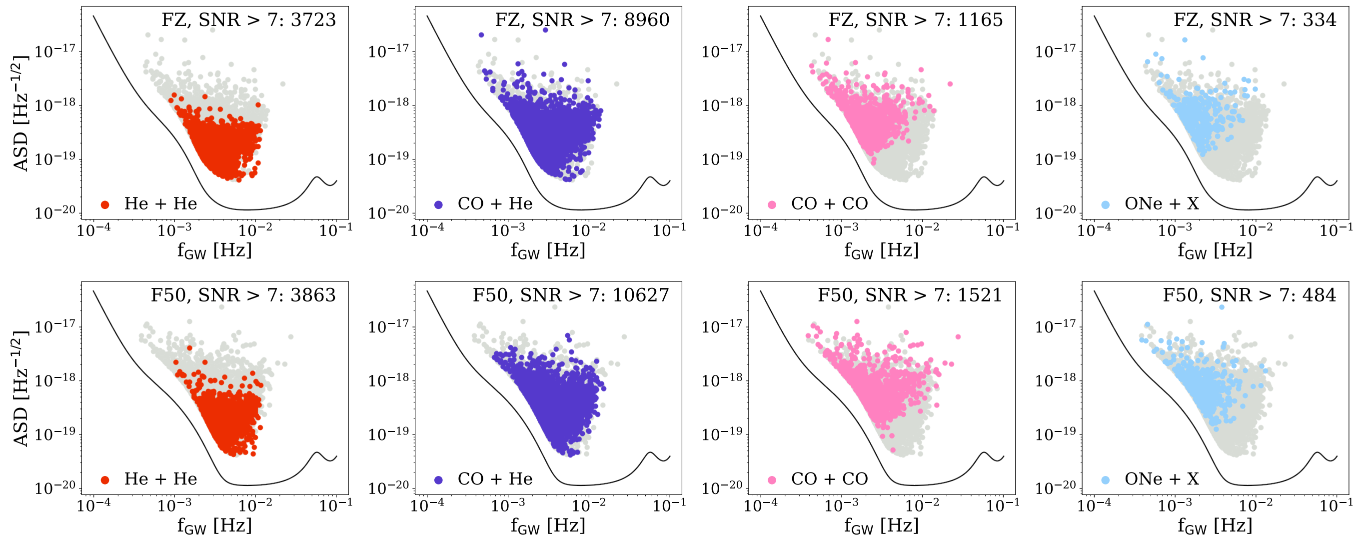

Figure 6. The ASD vs GW frequency for DWDs resolved with SNR > 7 for each DWD type where the top row shows the population from model FZ and the bottom row shows the population from model F50. In each panel, the LISA sensitivity curve, including the confusion foreground for each model, is shown in black and the total population for each model is shown in grey. We find that each model qualitatively exhibits similar characteristics and that the only change is in the yield of resolved DWDs for each type based on the strength of the confusion foreground.

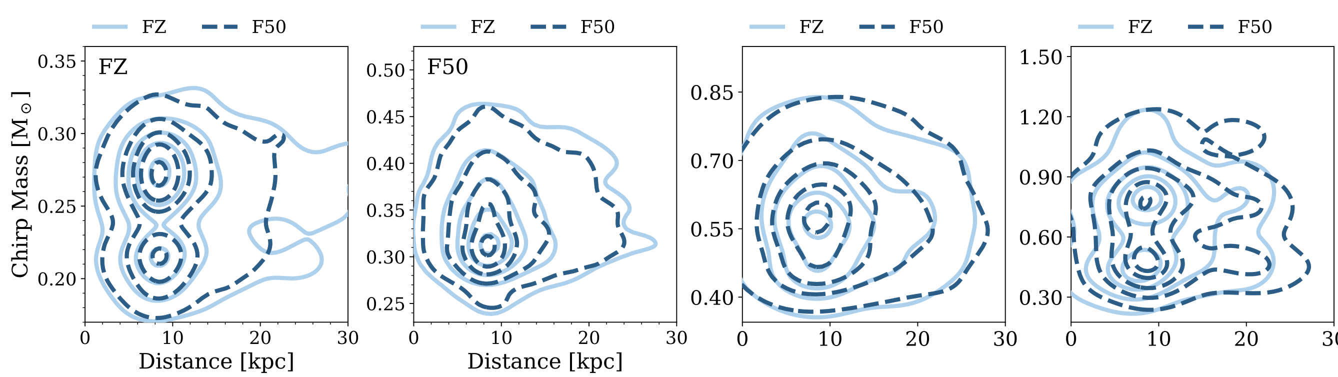

Figure 7. The chirp mass vs distance for each DWD type is shown. Only systems with observable evolution in their GW frequency, i.e those which are chirping, and with SNR > 7, are shown, since these are systems for which distance can be separated from chirp mass within their strain amplitude. Each panel shows one DWD type, summed over all metallicities. Model FZ is indicated with solid light blue contours, and model F50 is indicated with dark blue dashed contours respectively. Contours are shown at the 5$^{\rm th}$, 25$^{\rm th}$, 50$^{\rm th}$, 75$^{\rm th}$, and 95$^{\rm th}$ percentiles. Despite intrinsic changes to population properties induced by a metallicity-dependent binary fraction, and a reduction in the height of the DWD Galactic foreground the distributions are very similar.

The distance and chirp mass of DWDs which exhibit observable orbital evolution due to the emission of GWs during the LISA mission can be measured. This is because the chirp mass – distance degeneracy in the observed strain can be broken with the observed GW frequency evolution, or chirp. Assuming a chirp resolution of $1/T_{\rm obs}^2 \sim 8 \times 10^{-9}\,{\rm Hz}^2$, we select the DWDs whose chirp masses and distances can be measured. Figure 7 shows the chirp mass vs the luminosity distance for each DWD type in this selected population. The contours show the 5$^{\rm th}$, 25$^{\rm th}$, 50$^{\rm th}$, 75$^{\rm th}$, and 95$^{\rm th}$ percentiles for models FZ (light blue) and F50 (dark blue, dashed). Despite the reduction in the height of the confusion foreground when considering model FZ relative to F50, we find that LISA is unable to differentiate between the chirp mass – distance distributions of the two models.

6. BINARY EVOLUTION PARAMETER VARIATIONS

In order to test the robustness of the reduction of the height of the Galactic DWD GW foreground when assuming a metallicity-dependent binary fraction, we re-

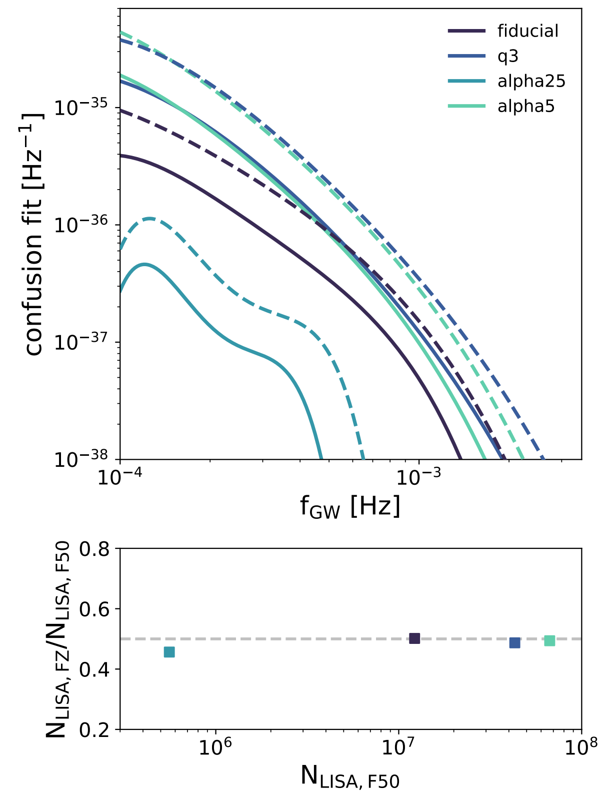

Figure 8. The top panel shows the Galactic DWD confusion fit vs GW frequency for different binary evolution **parameter variations** (colors) with model F50 shown in dashed lines and model FZ shown in solid lines. The bottom panel shows the ratio of the number of DWDs orbiting in the LISA frequency band for model FZ to model F50 vs to number of DWDs orbiting in the LISA band for model F50 only. While both the height of the confusion foreground and number of LISA DWDs changes for each variation, the FZ models within each variation exhibit a constant reduction by a factor of two compared with the F50 models.

peat our analysis using three different binary evolution **parameter variations**. For each variation, we consider models FZ and F50 as done in the fiducial case described above. In variation $q3$, we vary the assumption for the critical mass ratios at which a RLO interaction remains stable or becomes unstable from our fiducial assumptions such that the critical mass ratio is increased to 3.0 and thus allows stable mass transfer for more massive RLO donors. In variations $\alpha 25$ and $\alpha 5$, we modify the common envelope ejection efficiency to be either much less ($\alpha = 0.25$) or more ($\alpha = 5$) than in our fiducial assumption ($\alpha = 1$). Larger common envelope ejection efficiencies lead to wider post-CE separations, while smaller ejection efficiencies either lead to closer post-CE separations or mergers where the envelope ejection fails.

In each variation, changing the binary evolution assumptions dramatically changes the formation and evolution of the DWD populations. These changes lead to large shifts in the overall number of close DWDs in our synthetic present-day Milky-Way-like galaxies. We find that the total number of DWDs with $f_{\rm GW} > 10^{-4}$ Hz increases for both variations $q3$ and $\alpha 5$. This is because there are fewer stellar mergers which occur before the formation of a DWD, thus allowing more systems to evolve due to GW emission and orbit in the LISA frequency band at present. Conversely, for variation $\alpha 0.25$, we find that the number of DWDs orbiting with frequencies in the LISA band is drastically reduced. This is because of the highly inefficient use of orbital energy to eject the common envelope, thus producing more stellar mergers, or closer binaries which are more prone to future mergers.

Interestingly, when we compare the populations of each binary fraction model for our variations, we find that the number of close DWDs reduces by the constant factor of two as seen in our fiducial set of assumptions. This is illustrated in 8. The top panel shows the confusion foreground fits for each binary evolution variation (different colored lines) and for each binary fraction model where the solid lines show FZ models and dotted lines show F50 models. The bottom panel shows the ratio of the number of DWDs orbiting in the LISA frequency band for the FZ models vs the F50 models for each variation. Even though the number of DWDs in the LISA band spans over two orders of magnitude, the ratio of FZ to F50, as well as the spectral shape of the confusion fit, stays fixed at a constant factor of two reduction. This suggests that assuming a metallicity-dependent binary fraction reduces the size of the Galactic close DWD population by a factor of $\sim$ two and the strength of the Galactic DWD GW foreground for LISA *regardless of the chosen binary evolution model.*

7. CONCLUSIONS

In this study, we have investigated the effects of assuming a metallicity-dependent binary fraction on the formation and evolution of the Galactic population of DWDs with a special focus on the implications for LISA. Based on our synthetic Milky-Way-like galaxy catalogs of DWDs, we find that applying a metallicity-dependent binary fraction changes the formation efficiency and evolutionary history of DWD populations. However, when considering the close DWD populations observable by LISA, we find that the only distinguishing features between models which assume a metallicity-dependent binary fraction (model FZ) and models which assume a flat 50% binary fraction (model F50) are the population sizes and the strength of the Galactic DWD GW foreground. Models which assume a metallicity-dependent binary fraction produce Galactic DWD populations that are reduced by a factor of two relative to the standard model assumptions. This reduction extends to the height of the confusion foreground in the LISA data stream.

We extended our study to include three binary evolution **parameter variations** to investigate whether the DWD population reduction was robust to changes in assumptions for mass transfer stability and common envelope ejection efficiencies. While our binary evolution **parameter variations** change the size of the LISA-observable populations dramatically, the reduction in the size of the close Galactic DWD population and the height of the confusion foreground for models which assume a metallicity-dependent binary fraction is robust. An important consequence of a lower Galactic DWD confusion foreground is that relative to the total DWD population, more DWDs can be individually resolved because of the reduction in competing GW signals. While the number of DWDs radiating GWs in the LISA frequency band is reduced by a factor of two for model FZ relative to model F50, the number of resolved sources is less affected with a population-wide reduction of 14%. These results are far-reaching since the strength of the Galactic DWD confusion foreground has direct consequences on the detectability of all other LISA sources with small SNRs. An increase in resolution capability from the reduced confusion foreground can be extended to other galactic binaries that LISA will observe at these frequencies like those involving neutron stars and stellar-origin black holes, as well as other more exotic GW sources like merging supermassive black holes, extreme mass ratio inspirals, or cosmological GW backgrounds. Based on our results, we suggest that studies which employ fits to the confusion foreground based on population synthesis results consider reducing the strength of the Galactic foreground PSD by a factor of two.

The authors are grateful for helpful discussions with Carles Badenes, Christine Mazzola Daher, and the Gravitational Waves and Astronomical Data groups at the CCA. The authors are also grateful to the referee for providing a thoughtful review which strengthened the presentation of the manuscript. S.T. was supported by an Undergraduate Student Research Award (USRA) at CITA from the Natural Sciences and Engineering Research Council of Canada (NSERC), Reference # 498223. K.B. is grateful for support from the Jeffrey L. Bishop Fellowship. The Flatiron Institute is supported by the Simons Foundation.

DATA AVAILABILITY

All data and software required to reproduce our results are available through GitHub and Zenodo which are accessible through the icon links associated with our abstract and each figure.

Software: `astropy` (Astropy Collaboration et al. 2013; Price-Whelan et al. 2018); `COSMIC` (Breivik et al. 2020b); `LEGWORK` (Wagg et al. 2021); `matplotlib` (Hunter 2007); `numpy` (van der Walt et al. 2011); `pandas` (Wes McKinney 2010; pandas development team 2020); `scipy` (Jones et al. 2001)

REFERENCES

Adams, M. R., & Cornish, N. J. 2014, PhRvD, 89, 022001, doi: 10.1103/PhysRevD.89.022001

Amard, L., & Matt, S. P. 2020, The Astrophysical Journal, 889, 108, doi: 10.3847/1538-4357/ab6173

Amard, L., Palacios, A., Charbonnel, C., et al. 2019, A&A, 631, A77, doi: 10.1051/0004-6361/201935160

Amaro-Seoane, P., Audley, H., Babak, S., et al. 2017, arXiv e-prints, arXiv:1702.00786. https://arxiv.org/abs/1702.00786

Astropy Collaboration, Robitaille, T. P., Tollerud, E. J., et al. 2013, A&A, 558, A33, doi: 10.1051/0004-6361/201322068

Babak, S., Gair, J., Sesana, A., et al. 2017, PhRvD, 95, 103012, doi: 10.1103/PhysRevD.95.103012

Badenes, C., Mazzola, C., Thompson, T. A., et al. 2018, ApJ, 854, 147, doi: 10.3847/1538-4357/aaa765

Barack, L., & Cutler, C. 2007, PhRvD, 75, 042003, doi: 10.1103/PhysRevD.75.042003

Bartolo, N., Caprini, C., Domcke, V., et al. 2016, JCAP, 2016, 026, doi: 10.1088/1475-7516/2016/12/026

Bellovary, J. M., Cleary, C. E., Munshi, F., et al. 2019, MNRAS, 482, 2913, doi: 10.1093/mnras/sty2842

Benacquista, M., & Holley-Bockelmann, K. 2006, ApJ, 645, 589, doi: 10.1086/504024

Berti, E., Cardoso, V., & Will, C. M. 2006, PhRvD, 73, 064030, doi: 10.1103/PhysRevD.73.064030

Boileau, G., Lamberts, A., Christensen, N., Cornish, N. J., & Meyer, R. 2021, MNRAS, 508, 803, doi: 10.1093/mnras/stab2575

Breivik, K., Kremer, K., Bueno, M., et al. 2018, ApJL, 854, L1, doi: 10.3847/2041-8213/aaaa23

Breivik, K., Mingarelli, C. M. F., & Larson, S. L. 2019, Constraining Galactic Structure with the LISA White Dwarf Foreground, arXiv, doi: 10.48550/ARXIV.1912.02200

Breivik, K., Mingarelli, C. M. F., & Larson, S. L. 2020a, ApJ, 901, 4, doi: 10.3847/1538-4357/abab99

Breivik, K., Coughlin, S., Zevin, M., et al. 2020b, ApJ, 898, 71, doi: 10.3847/1538-4357/ab9d85

Caldwell, R. R., Smith, T. L., & Walker, D. G. E. 2019, PhRvD, 100, 043513, doi: 10.1103/PhysRevD.100.043513

Caprini, C., Hindmarsh, M., Huber, S., et al. 2016, JCAP, 2016, 001, doi: 10.1088/1475-7516/2016/04/001

Chatziioannou, K., Clark, J. A., Bauswein, A., et al. 2017, PhRvD, 96, 124035, doi: 10.1103/PhysRevD.96.124035

Claeys, J. S. W., Pols, O. R., Izzard, R. G., Vink, J., & Verbunt, F. W. M. 2014, A&A, 563, A83, doi: 10.1051/0004-6361/201322714

Cornish, N. J. 2020, PhRvD, 102, 124038, doi: 10.1103/PhysRevD.102.124038

de Mink, S. E., Pols, O. R., & Hilditch, R. W. 2007, A&A, 467, 1181, doi: 10.1051/0004-6361:20067007

Eggleton, P. P. 1983, ApJ, 268, 368, doi: 10.1086/160960

Flanagan, É. É., & Hughes, S. A. 1998, PhRvD, 57, 4535, doi: 10.1103/PhysRevD.57.4535

Geller, A. M., Leigh, N. W. C., Giersz, M., Kremer, K., & Rasio, F. A. 2019, ApJ, 872, 165, doi: 10.3847/1538-4357/ab0214

Gokhale, V., Peng, X. M., & Frank, J. 2007, ApJ, 655, 1010, doi: 10.1086/510119

Goldberg, D., & Mazeh, T. 1994, A&A, 282, 801

Hopkins, P. F. 2015, MNRAS, 450, 53, doi: 10.1093/mnras/stv195

Hopkins, P. F., Wetzel, A., Kereš, D., et al. 2018, MNRAS, 480, 800, doi: 10.1093/mnras/sty1690

Hunter, J. D. 2007, Computing in Science and Engineering, 9, 90, doi: 10.1109/MCSE.2007.55

Hurley, J. R., Pols, O. R., & Tout, C. A. 2000, MNRAS, 315, 543, doi: 10.1046/j.1365-8711.2000.03426.x

Hurley, J. R., Tout, C. A., & Pols, O. R. 2002, MNRAS, 329, 897, doi: 10.1046/j.1365-8711.2002.05038.x

Jayasinghe, T., Kochanek, C. S., Strader, J., et al. 2021, MNRAS, 506, 4083, doi: 10.1093/mnras/stab1920

Jones, E., Oliphant, T., Peterson, P., et al. 2001, SciPy: Open source scientific tools for Python. http://www.scipy.org/

Kilic, M., Bédard, A., & Bergeron, P. 2021, MNRAS, 502, 4972, doi: 10.1093/mnras/stab439

Klein, A., Barausse, E., Sesana, A., et al. 2016, PhRvD, 93, 024003, doi: 10.1103/PhysRevD.93.024003

Korol, V., Hallakoun, N., Toonen, S., & Karnesis, N. 2021, arXiv e-prints, arXiv:2109.10972. https://arxiv.org/abs/2109.10972

Korol, V., Koop, O., & Rossi, E. M. 2018, ApJL, 866, L20, doi: 10.3847/2041-8213/aae587

Korol, V., Rossi, E. M., & Barausse, E. 2019, MNRAS, 483, 5518, doi: 10.1093/mnras/sty3440

Korol, V., Rossi, E. M., Groot, P. J., et al. 2017, MNRAS, 470, 1894, doi: 10.1093/mnras/stx1285

Kremer, K., Breivik, K., Larson, S. L., & Kalogera, V. 2017, ApJ, 846, 95, doi: 10.3847/1538-4357/aa8557

Kremer, K., Sepinsky, J., & Kalogera, V. 2015, ApJ, 806, 76, doi: 10.1088/0004-637X/806/1/76

Kroupa, P. 2001, MNRAS, 322, 231, doi: 10.1046/j.1365-8711.2001.04022.x

Lamberts, A., Blunt, S., Littenberg, T. B., et al. 2019, MNRAS, 490, 5888, doi: 10.1093/mnras/stz2834

Leiner, E. M., & Geller, A. 2021, ApJ, 908, 229, doi: 10.3847/1538-4357/abd7e9

Littenberg, T. B., Cornish, N. J., Lackeos, K., & Robson, T. 2020, PhRvD, 101, 123021, doi: 10.1103/PhysRevD.101.123021

Mandhai, S., Lamb, G. P., Tanvir, N. R., et al. 2021, arXiv e-prints, arXiv:2109.09714. https://arxiv.org/abs/2109.09714

Marsh, T. R., Nelemans, G., & Steeghs, D. 2004, MNRAS, 350, 113, doi: 10.1111/j.1365-2966.2004.07564.x

Mazeh, T., Goldberg, D., Duquennoy, A., & Mayor, M. 1992, ApJ, 401, 265, doi: 10.1086/172058

Mazzola, C. N., Badenes, C., Moe, M., et al. 2020, MNRAS, 499, 1607, doi: 10.1093/mnras/staa2859

Moe, M., & Di Stefano, R. 2017, ApJS, 230, 15, doi: 10.3847/1538-4365/aa6fb6

Moe, M., Kratter, K. M., & Badenes, C. 2019, ApJ, 875, 61, doi: 10.3847/1538-4357/ab0d88

Moore, C. J., Chua, A. J. K., & Gair, J. R. 2017, Classical and Quantum Gravity, 34, 195009, doi: 10.1088/1361-6382/aa85fa

Nelemans, G., Yungelson, L. R., Portegies Zwart, S. F., & Verbunt, F. 2001, A&A, 365, 491, doi: 10.1051/0004-6361:20000147

Nissanke, S., Vallisneri, M., Nelemans, G., & Prince, T. A. 2012, ApJ, 758, 131, doi: 10.1088/0004-637X/758/2/131

pandas development team, T. 2020, pandas-dev/pandas: Pandas, 1.1.1, Zenodo, doi: 10.5281/zenodo.3509134

Peters, P. C. 1964, Physical Review, 136, 1224, doi: 10.1103/PhysRev.136.B1224

Price-Whelan, A. M., Sipőcz, B. M., Günther, H. M., et al. 2018, AJ, 156, 123, doi: 10.3847/1538-3881/aabc4f

Price-Whelan, A. M., Hogg, D. W., Rix, H.-W., et al. 2020, ApJ, 895, 2, doi: 10.3847/1538-4357/ab8acc

Robson, T., Cornish, N. J., & Liu, C. 2019, Classical and Quantum Gravity, 36, 105011, doi: 10.1088/1361-6382/ab1101

Ruiter, A. J., Belczynski, K., Benacquista, M., Larson, S. L., & Williams, G. 2010, The Astrophysical Journal, 717, 1006, doi: 10.1088/0004-637x/717/2/1006

Sanderson, R. E., Wetzel, A., Loebman, S., et al. 2020, ApJS, 246, 6, doi: 10.3847/1538-4365/ab5b9d

Sepinsky, J. F., & Kalogera, V. 2014, ApJ, 785, 157, doi: 10.1088/0004-637X/785/2/157

Shen, K. J. 2015, ApJL, 805, L6, doi: 10.1088/2041-8205/805/1/L6

Soberman, G. E., Phinney, E. S., & van den Heuvel, E. P. J. 1997, A&A, 327, 620. https://arxiv.org/abs/astro-ph/9703016

Stephan, A. P., Naoz, S., Ghez, A. M., et al. 2019, ApJ, 878, 58, doi: 10.3847/1538-4357/ab1e4d

Toonen, S., Nelemans, G., & Portegies Zwart, S. 2012, A&A, 546, A70, doi: 10.1051/0004-6361/201218966

Tout, C. A., Aarseth, S. J., Pols, O. R., & Eggleton, P. P. 1997, MNRAS, 291, 732, doi: 10.1093/mnras/291.4.732

Valsecchi, F., Farr, W. M., Willems, B., Deloye, C. J., & Kalogera, V. 2012, ApJ, 745, 137, doi: 10.1088/0004-637X/745/2/137

van der Walt, S., Colbert, S. C., & Varoquaux, G. 2011, Computing in Science and Engineering, 13, 22, doi: 10.1109/MCSE.2011.37

Vink, J. S., de Koter, A., & Lamers, H. J. G. L. M. 2001, A&A, 369, 574, doi: 10.1051/0004-6361:20010127

Wagg, T., Breivik, K., & de Mink, S. E. 2021, arXiv e-prints, arXiv:2111.08717. https://arxiv.org/abs/2111.08717

Wang, H., Stephan, A. P., Naoz, S., Hoang, B.-M., & Breivik, K. 2021, ApJ, 917, 76, doi: 10.3847/1538-4357/ac088d

Webbink, R. F. 1985, Stellar evolution and binaries, ed. J. E. Pringle & R. A. Wade, 39

Wes McKinney. 2010, in Proceedings of the 9th Python in Science Conference, ed. Stéfan van der Walt & Jarrod Millman, 56 – 61, doi: 10.25080/Majora-92bf1922-00a

Wetzel, A. R., Hopkins, P. F., Kim, J.-h., et al. 2016, ApJL, 827, L23, doi: 10.3847/2041-8205/827/2/L23

Wong, K. W. K., Breivik, K., Kremer, K., & Callister, T. 2021, PhRvD, 103, 083021, doi: 10.1103/PhysRevD.103.083021

Yu, S., & Jeffery, C. S. 2013, MNRAS, 429, 1602, doi: 10.1093/mnras/sts445

Zevin, M., Kelley, L. Z., Nugent, A., et al. 2020a, ApJ, 904, 190, doi: 10.3847/1538-4357/abc266

Zevin, M., Spera, M., Berry, C. P. L., & Kalogera, V. 2020b, ApJL, 899, L1, doi: 10.3847/2041-8213/aba74e

Zevin, M., Bavera, S. S., Berry, C. P. L., et al. 2021, ApJ, 910, 152, doi: 10.3847/1538-4357/abe40e